Nanoscale temperature mapping in operating microelectronic devices

Matthew Mecklenburg,[1*] William A. Hubbard[2], E. R. White,[2]
Rohan Dhall,[3] Stephen B. Cronin,[3] Shaul Aloni,[4] B. C. Regan[2*]

[1]Center for Electron Microscopy and Microanalysis, University of Southern California,
Los Angeles, California, 90089

[2]Department of Physics and Astronomy, University of California,
Los Angeles, California, 90095

California NanoSystems Institute, University of California,
Los Angeles, California, 90095

[3]Department of Electrical Engineering, University of Southern California,
Los Angeles, California, 90089

[4]Molecular Foundry, Lawrence Berkeley National Laboratory,
Berkeley, CA 94720, USA

*Corresponding author. E-mail:
matthew.mecklenburg@usc.edu (M.M.); regan@physics.ucla.edu (B.C.R.).

Modern microelectronic devices have nanoscale features that dissipate power non-uniformly, but fundamental physical limits frustrate efforts to detect the resulting temperature gradients. Contact thermometers disturb the temperature of a small system, while radiation thermometers struggle to beat the diffraction limit. Exploiting the same physics as Fahrenheit's glass-bulb thermometer, we mapped the thermal expansion of Joule-heated, 80 nanometer-thick aluminum wires by precisely measuring changes in density. With a scan-

ning transmission electron microscope (STEM) and electron energy loss spectroscopy (EELS), we quantified the local density via the energy of aluminum's bulk plasmon. Rescaling density to temperature yields maps with a statistical precision of 3 kelvin/hertz$^{-1/2}$, an accuracy of 10%, and nanometer-scale resolution. Many common metals and semiconductors have sufficiently sharp plasmon resonances to serve as their own thermometers.

Long before thermodynamic temperature was understood, it was defined as a measurable quantity in terms of the thermal expansion of air, red wine, alcohol, or mercury-in-glass. Now temperature T is considered to be a statistical concept, defined by the derivative of a system's entropy S with respect to its energy E according to $T^{-1} \equiv \partial S/\partial E$ (*1*). This understanding is challenged in highly-localized (*2*) or non-equilibrium (*3*) systems, where the standard statistical reasoning is difficult to apply. Small systems are also problematic from a practical standpoint. Contact thermometers (such as thermocouples) require a thermal connection that disturbs a small system's temperature (*4, 5*). Non-contact thermometers based on the detection of radiation, whether thermal (*6*), Raman (*7*), reflected (*8*), or luminescent (*5, 9*), naturally have their spatial resolution limited by the wavelengths of the radiation detected (*4, 5*). In modern semiconductor devices, millions of transistors generate thermal gradients on length scales that are tiny compared to infrared and optical wavelengths (*10*). Thus thermometric techniques with high spatial resolution are applicable to important problems ranging from the statistical foundations of thermodynamics (*2, 3*) to heat management in microprocessors (*5, 10, 11*).

High-spatial-resolution thermometry is under constant development in many arenas (*5*). Some approaches involve inserting local probes [even miniature expansion thermometers (*12*)] that can be queried remotely. For instance, luminescent nanoparticles inserted in biological systems can measure intracellular temperature gradients (*9*), or low-melting point metals deposited on a solid-state device can provide a binary temperature determination (*13, 14*). Alternatively,

the thermometer can be external and mobile. Scanning probe techniques include scanning thermal microscopy (SThM), where the tip of an atomic force microscope is equipped with a thermocouple or resistive sensor (*15, 16*), and near-field scanning optical microscopy, where a fiber is employed to beat the far-field diffraction limit (*4,5,11,17*). Both of these methods can achieve resolution $\lesssim 50$ nm (*16, 17*). Perhaps most like the work described here, nuclear magnetic resonance (NMR) (*18*), electron backscatter diffraction (*19*), or inelastic electron scattering (*20*) can induce the measured system to provide its own thermometric signal. Of these three, only the NMR technique has demonstrated mapping with millimeter-scale resolution (*18*). Of all of the aforementioned methods, none have demonstrated detailed temperature maps with sub-10 nm spatial resolution.

Here we describe a non-contact, thermometric technique that can measure bulk temperatures with nanometer-scale spatial resolution: plasmon energy expansion thermometry (PEET). Based on electron energy loss spectroscopy (EELS), the technique is non-contact in the sense that the measurement has negligible effect on the measured system's temperature. Like Fahrenheit's mercury-in-glass thermometer, this thermometer derives its sensitivity and accuracy from the calibrated thermal expansion of a convenient material, here aluminum. As outlined in Fig. 1A, we apply EELS in a scanning transmission electron microscope (STEM) to measure the energy E required to excite a bulk plasmon in the metal. In the free-electron model, this energy is given by

$$E = \hbar\omega_p = \hbar\sqrt{\frac{4\pi ne^2}{m}}, \tag{1}$$

where $\hbar$ is the reduced Planck constant, ω_p is the plasmon angular frequency, and n is the number density of valence electrons with charge e and mass m. At room temperature (T_0), aluminum has $n(T_0) \simeq 1.8 \times 10^{29}$ m^{-3}, which gives $E(T_0) \simeq 15.8\,e$V according to Eq. (1). This value is within 3% of the measured value of 15.2 eV (*21*), demonstrating the applicability of the free electron model in aluminum.

The plasmon energy is temperature-sensitive because thermal expansion changes the number density according to $n(T) \simeq n(T_0)[1 - 3f(T)]$, where $f(T) \equiv \int_{T_0}^{T} \alpha(T')dT' \simeq \alpha_1\Delta T + \alpha_2\Delta T^2$ and α is the coefficient of linear thermal expansion (21–23). The normalized change in the plasmon energy $R \equiv (E(T) - E(T_0))/E(T_0)$ is thus related to the temperature change ΔT by a quadratic equation with solution

$$\Delta T \equiv T - T_0 = \frac{\alpha_1}{2\alpha_2}\left(\sqrt{1 - \frac{8R\alpha_2}{3\alpha_1^2}} - 1\right). \tag{2}$$

In aluminum the coefficients $\alpha_1 = 23.5 \times 10^{-6}$ K^{-1} and $\alpha_2 = 8.9 \times 10^{-9}$ K^{-2} approximate (24) $f(T)$ to better than 2% over the range from 25 to 650°C (25). By focusing the STEM electron beam into a nanometer-sized probe, rastering it over the sample, and analyzing the shift of the plasmon peak in the EELS spectrum according to Eq.(2), we produce a temperature map.

With a plasmon peak width ~ 1.3 eV, the peak shift of roughly -0.54 meV/K (in the linear approximation) is too subtle to reliably detect by merely locating the peak maximum. However, curve-fitting [see Methods (26)] improves our sensitivity to energy or temperature shifts by almost an order of magnitude. Figure 1B shows the shift for a large (120 K) temperature difference, measured with a spectrum integration time of 26 ms. Under such imaging conditions, repeated measurements at a single point give standard deviations in the energy loss of 8 to 12 meV, which is equivalent to 15 to 21 K. For spectrum acquisition rates of 38 to 76 s^{-1}, our plasmon energy sensitivity scales like shot noise with slope ~ 1.7 m$eV/\sqrt{\text{Hz}}$, equivalent to 3 K$/\sqrt{\text{Hz}}$.

To demonstrate PEET's spatial resolution, we used electron-beam lithography to fabricate a variety of serpentine aluminum devices that exhibit temperature gradients on sub-micron temperature scales (Fig. 1C). Depending on the contacts used, a device can be Joule-heated locally by applying a voltage across it, or remotely by heating its neighbor [see Methods (26)].

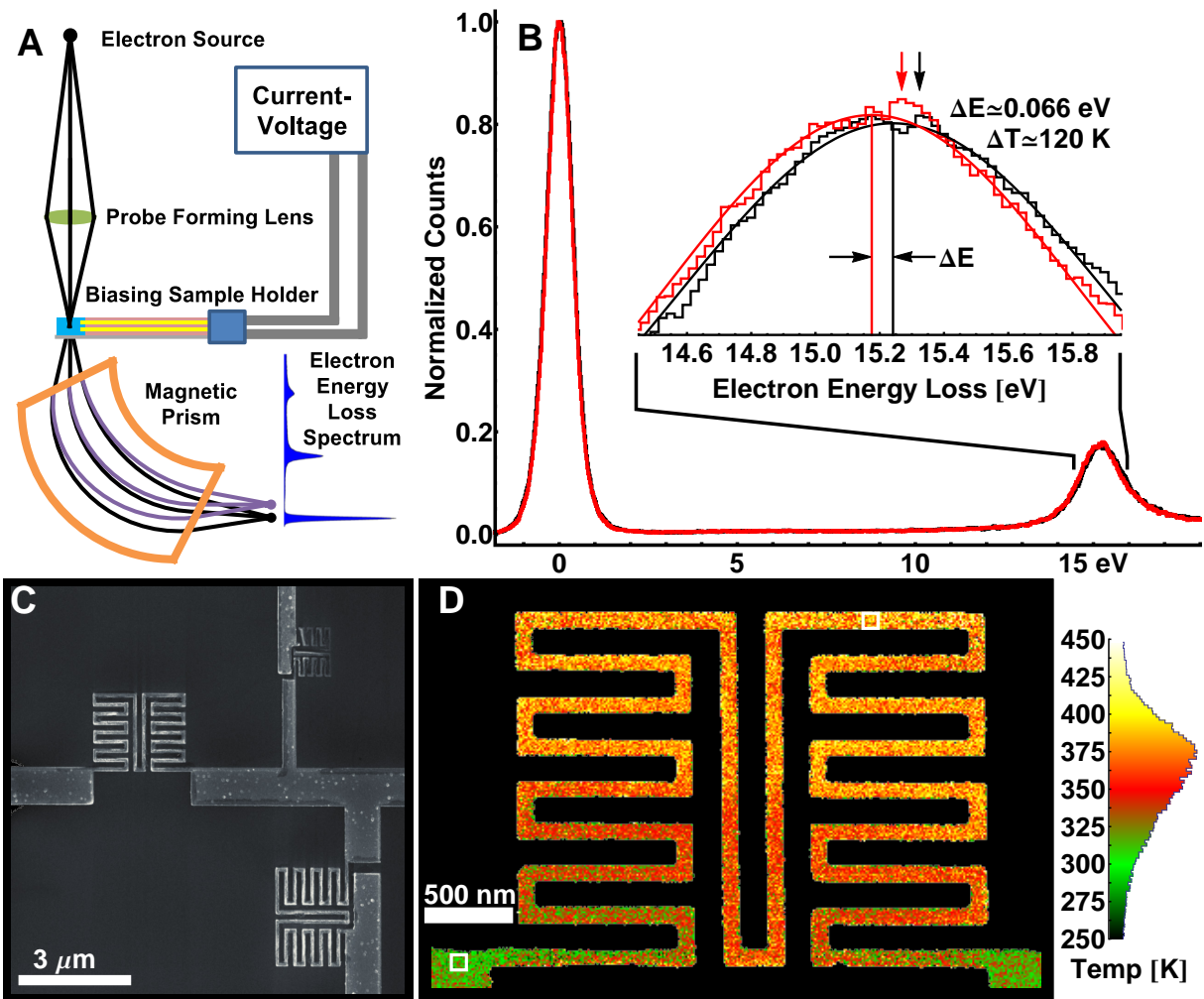Local heating gives PEET maps such as Fig. 1D. The map contains 336 by 223 pixels

Figure 1: **Experiment overview.** **(A)** Apparatus: a STEM, a biasing sample holder, a power source for Joule-heating the sample, and an EELS spectrometer. **(B)** Aluminum EELS data characteristic of 293 K (black) and 413 K (red). The vertical lines in the inset indicate the plasmon peak centers, as determined by curve-fitting, while the arrows indicate the peak maxima. **(C)** Scanning electron microscope image of an example device architecture. Four leads connect to three Al device geometries over an electron-transparent, Si_3N_4 membrane. **(D)** A false-color temperature map of a 80-nm-thick, 100 nm-wide serpentine aluminum wire Joule-heated by the application of 161 μA. The histogram indicates the color scale and bins each pixel according to its temperature. The average temperatures measured in the indicated 86 nm by 86 nm squares are 310 ± 2 K (lower-left) and 390 ± 3 K (upper right).

5

with an 11 nm pitch, and is derived from two EELS spectrum images, one acquired at room temperature and the other at elevated temperature. Thus each pixel has two associated spectra like those shown in Fig. 1B. Averaging over 64 pixels in the indicated square regions gives standard errors of 2 and 3 K respectively, showing a temperature difference 80 ± 4 K with a signal-to-noise ratio of 20. The highest temperatures are not found at the wire's midpoint, as would be expected for a straight and uniform 1D conductor, but rather in the sections farthest from the lead connections. PEET reveals that the midpoint loses heat to the cooler end legs (only 150 nm away) through the Si_3N_4 membrane and via near-field electromagnetic transport (*11*).

The PEET analysis procedure is described in more detail in Fig. 2, which shows raw maps of the plasmon energy for a device with zero (Fig. 2A) and non-zero (Fig. 2B) power applied to a remote heater. In both cases the sensitive curve-fitting procedure reveals nanometer-scale structures in the aluminum. Most noticeable in the leads, these structures are due to grain boundaries, which show a plasmon energy decrease of $\Delta E = 13 \pm 12$ meV (Figs. S1 and S2). The implied density decrease of $\Delta n/n \simeq 2\Delta E/E \simeq 0.2\%$ is expected because of the grain boundary volume excess (*27*). Without correction the grain boundary shift would give a false temperature offset of ~ 24 K. The subtraction in the normalized plasmon shift ratio $R = $ (B-A)/A (where the letters refer to the respective panels of Fig. 2) suppresses this potential systematic, leaving residuals that are barely evident in the temperature map in Fig. 2C (Fig. S3).

The map in Fig. 2C shows a steady warming with distance from the lower contact, a trend easier to appreciate quantitatively in the seven line profiles 2D. With a spectrum acquisition rate of 76 s^{-1}, each map pixel has a statistical uncertainty of 26 K. The histograms 2E show that the mean temperature difference ~ 30 K between each horizontal leg and its neighbor is resolved. Furthermore, the topmost and bottommost profiles have standard deviations that are comparable to the expected 8 K statistical noise, whereas the other histograms are generally broadened, reflecting the significant temperature gradients in the horizontal legs and the absence
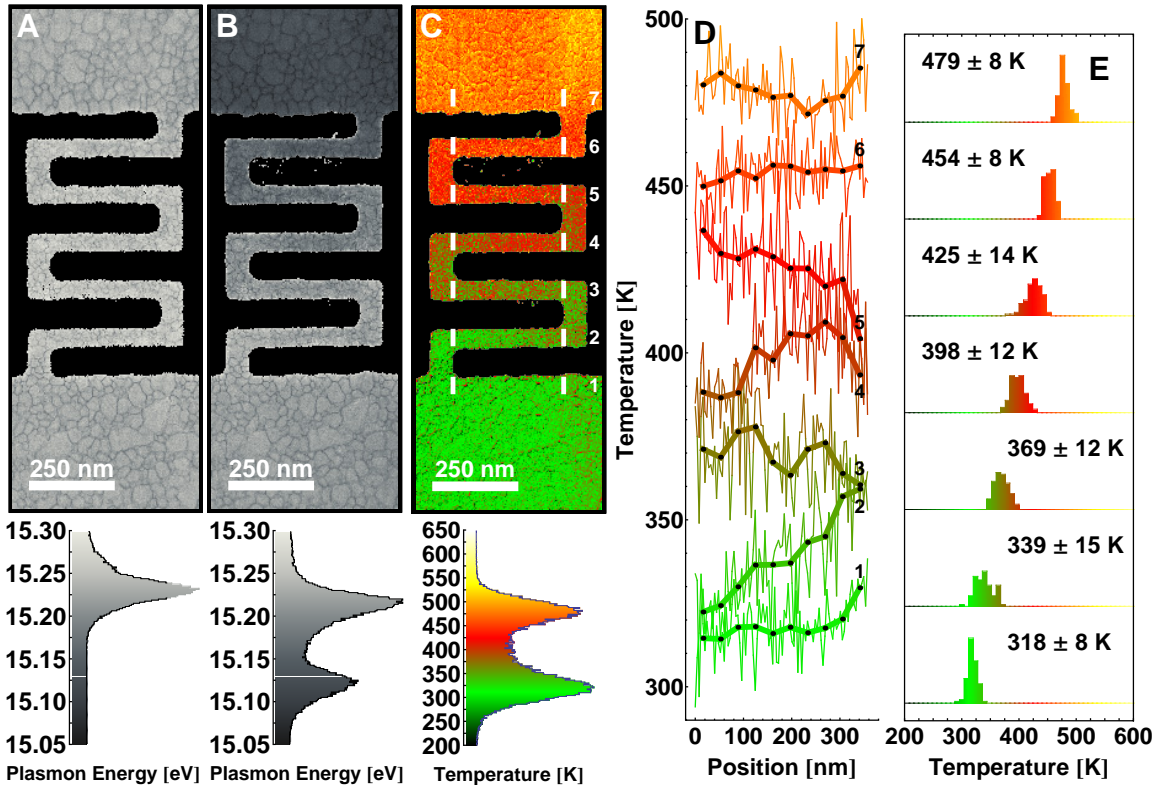
Figure 2: **Remote heating:** Plasmon energy map with 4-nm pixels of a 100 nm-thick aluminum wire **(A)** at room temperature and **(B)** with 2 mW applied to a heater outside the field of view. **(C)** Temperature map constructed from **(A)** and **(B)**. White bars indicate the 90 by 10 pixel segments used to generate the line profiles **(D)** and histograms **(E)**. Narrow lines and histograms show data averaged over 40 nm vertically, while dots connected by thicker lines indicate data averaged over 40 nm in both directions.

of such gradients in the contacts.

In situ thermal studies with nanoscale thermometry can employ temperature control elements that are smaller, and thus faster. This advantage enables rapid heating and quenching experiments, and better control of systematics. For instance, annealing at elevated temperatures causes grain boundaries to reconfigure. But with a small heater over the electron-transparent window, the temperature can be cycled without pausing to wait for the thermal drift to stabilize. Thus the T_0 reference map can be frequently refreshed, mitigating this systematic without incurring a large duty-cycle penalty.

Figure 3 shows how the temperature of an aluminum contact, here heated remotely, can be changed by hundreds of degrees in real time, without disturbing the temperature measurement or causing the burdensome thermal drift typical of furnace-style heating sample holders. These data depict an EELS spectrum image acquisition where the power to the remote heater was ramped down in steps, with zero-power intervals separating each new non-zero value from the previous one (Fig. 3A). Heating effects are nearly undetectable in the annular dark field (ADF) images corresponding to zero power (Fig. 3C) and stepped-power (Fig. 3D). Grain rotation induced some tiny contrast changes, and the drift was sufficiently small to be handled by the EELS data acquisition software's automated drift correction routine, which executed every two rows.

Comparison of the ADF and plasmon energy images also emphasizes the common origin of the structure evident in the zero-power (T_0) images: grains. The ADF image shows diffraction contrast varying randomly from grain to grain based on the local lattice orientation, while the plasmon energy image highlights the grain boundaries because of the volume excess effect discussed above (see also Figs. S1 and S2). In the temperature map (Fig. 3G), a few grain boundaries show residuals 3–4 standard deviations from the mean (Fig. S3), but generally the grain boundary systematic is suppressed.
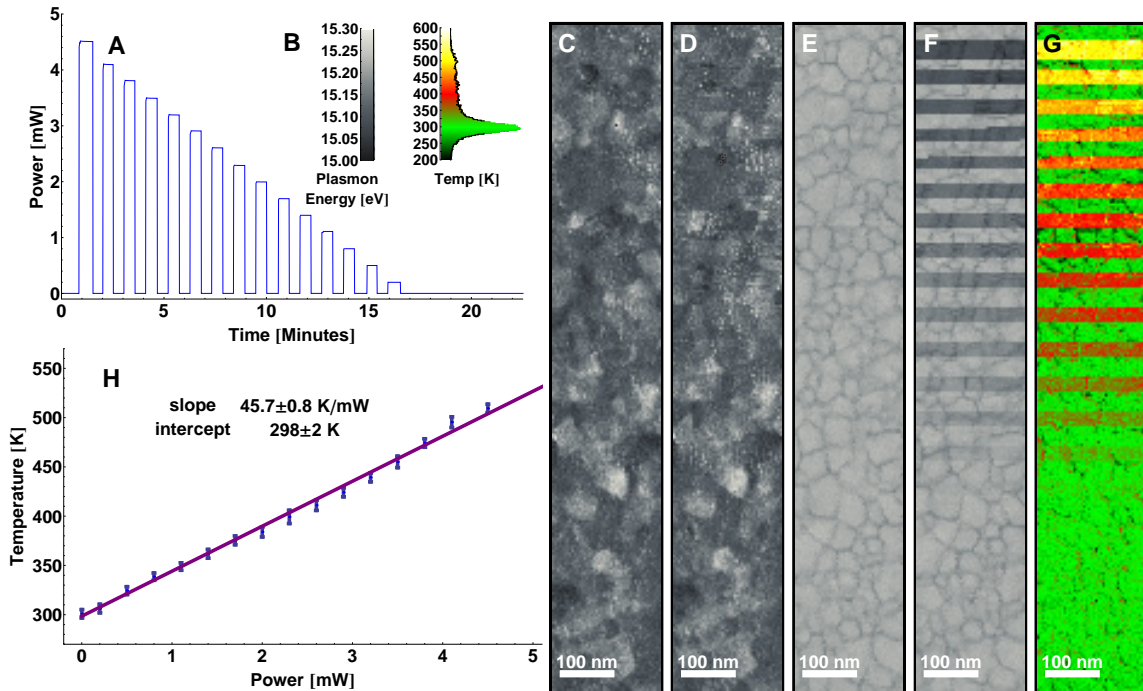
8

Figure 3: **Rapid, linear temperature changes:** **(A)** Remote heater power *vs.* time. **(B)** Plasmon energy scale for **(E, F)**, and a combination temperature scale and histogram of the pixels of **(G)**. **(C, D)** ADF STEM images corresponding to zero and variable power. In these 45 by 269 pixel images the beam was rastering from left to right, with a row time of 1.2 s, and then top to bottom. **(E, F)** Corresponding, simultaneously-acquired plasmon energy maps. **(G)** Temperature map constructed from the normalized subtraction of **(E)** from **(F)**. **(H)** Temperature extracted from **(G)** *vs.* heater power, along with a linear fit (red) and the corresponding fit parameters.

9

The abrupt transitions in the power-stepped plasmon energy (Fig. 3F) and temperature (Fig. 3G) maps demonstrate thermalization within a 26 ms pixel time. Although the field of view was nearly isothermal at any given instant, the effectively instantaneous temperature changes appear spatial because of the 22.5-min frame time. Figure 3G plots the mean temperature from each isothermal region as a function of the heater power. As expected for a small device in vacuum that is too cool to radiate appreciably, the temperature is linear in the applied power (*6*). When working either with devices or with lamellae deployed as local thermometers, a plot such as 3G is straightforward and fast to acquire, and it provides a translation between power and temperature that can be ported to situations where direct measurements of the latter are not feasible.

With careful calibration we expect sub-1 K accuracies are possible, because the physics underpinning PEET is well-understood on longer length scales (*21–23, 25*). (See also Figs. S4 to S8.) Heating by the electron beam is negligible. The temperature increment is roughly $\Delta T \simeq (I_b/e\kappa)(dE/dx)$ (*28*), where $I_b \simeq 0.5$ nA is the beam current and $\kappa \simeq 240$ W/K·m is aluminum's thermal conductivity. Plasmons, the dominant source of energy loss, are created by the beam in a mean free path $\ell_{\mathrm{PL}} \sim 100$ nm, which gives $dE/dx \sim 15\,e\mathrm{V}/(100$ nm). The resultant ΔT, less than 1 mK, is far below our current sensitivity. Using a furnace-style heating sample holder, we heated a sample from room temperature to 720 K, compared the PEET value with the holder's thermocouple reading, and found that they agree to within 10% (Fig. S4).

For the data presented here the rastering electron beam (probe) size was 1 to 2 nm, and the pixel spacing was as small as 2 nm (*26*). Is it meaningful to consider the existence of distinct temperatures at such small length scales in a solid, and can PEET measure them? Measurements of the plasmon energy do not sample distinct volumes for separations smaller than the plasmon delocalization length Λ_{pl}, which sets a resolution limit akin to the Rayleigh criterion (*29*). At 15.2 eV the plasmon delocalization is 3 nm (*29*), consistent with the grain boundary widths

(which correspond to atomic-scale features) seen in our plasmon energy maps (Fig. S1). However, the sample does not support a temperature gradient for separations smaller than the electron mean free path ℓ_e, because electrons are ballistic over distances less than ℓ_e. Thus, ℓ_e describes the smallest thermal feature size that can exist in continuous aluminum. Similarly, because phonons generate thermal expansion, temperature cannot produce different densities at separations smaller than a phonon mean free path $\ell_{\rm ph}$. We estimate $\ell_e \lesssim 4$ to 15 nm and $\ell_{\rm ph} \lesssim 2$ to 5 nm in our temperature range (see Table S1). For $\Lambda_{\rm pl}$ smaller than $\ell_{\rm ph}$ or ℓ_e, PEET achieves the maximum possible spatial resolution — temperature differences do not exist on length scales smaller than the larger mean free path.

PEET is applicable to many other technologically important metals and semiconductors. Tungsten, silver, silicon, gallium arsenide, and gallium nitride all have sufficiently sharp plasmon resonances (*29*). (The width of the plasmon resonance limits PEET's precision, so decreasing the ZLP width (*30*) gives only a small sensitivity improvement.) Because the product of the thermal expansion coefficient α with the melting temperature $\alpha T_m \sim 0.02$ for many materials (*31*), one will generally trade high sensitivity for a large accessible temperature range, or *vice versa*, depending on the application. Ideally the system to be measured serves as its own thermometer, without requiring the introduction of thermometric materials that might compromise the thermal behavior or device function.

References and Notes

1. F. Reif, *Fundamentals of statistical and thermal physics* (McGraw-Hill, New York, 1965).

2. M. Hartmann, G. Mahler, O. Hess, *Physical Review Letters* **93**, 080402 (2004).

3. Y. Dubi, M. Di Ventra, *Reviews of Modern Physics* **83**, 131 (2011).

4. J. Christofferson, *et al.*, *Journal of Electronic Packaging* **130**, 041101 (2008).

5. C. D. S. Brites, *et al.*, *Nanoscale* **4**, 4799 (2012).

6. S. B. Singer, M. Mecklenburg, E. R. White, B. C. Regan, *Physical Review B* **84**, 195468 (2011).

7. V. V. Deshpande, S. Hsieh, A. W. Bushmaker, M. Bockrath, S. B. Cronin, *Physical Review Letters* **102**, 105501 (2009).

8. G. Tessier, M. Bardoux, C. Boué, C. Filloy, D. Fournier, *Applied Physics Letters* **90**, 171112 (2007).

9. G. Kucsko, *et al.*, *Nature* **500**, 54 (2013).

10. E. Pop, S. Sinha, K. E. Goodson, *Proceedings of the IEEE* **94**, 1587 (2006).

11. D. G. Cahill, *et al.*, *Applied Physics Reviews* **1**, 011305 (2014).

12. Y. Gao, Y. Bando, *Nature* **415**, 599 (2002).

13. G. E. Begtrup, *et al.*, *Physical Review Letters* **99**, 155901 (2007).

14. T. Brintlinger, Y. Qi, K. H. Baloch, D. Goldhaber-Gordon, J. Cumings, *Nano Letters* **8**, 582 (2008).

15. M. Nonnenmacher, H. K. Wickramasinghe, *Applied Physics Letters* **61**, 168 (1992).

16. L. Shi, S. Plyasunov, A. Bachtold, P. L. McEuen, A. Majumdar, *Applied Physics Letters* **77**, 4295 (2000).

17. K. E. Goodson, M. Asheghi, *Microscale Thermophysical Engineering* **1**, 225 (1997).

18. N. N. Jarenwattananon, *et al.*, *Nature* **502**, 537 (2013).

19. X. Wu, R. Hull, *Nanotechnology* **23**, 465707 (2012).

20. S. B. Vendelbo, *et al.*, *Ultramicroscopy* **133**, 72 (2013).

21. H. Abe, M. Terauchi, R. Kuzuo, M. Tanaka, *Journal of Electron Microscopy* **41**, 465 (1992).

22. G. Meyer, *Zeitschrift für Physik* **148**, 61 (1957).

23. P. Palanisamy, J. M. Howe, *Journal of Applied Physics* **110**, 024908 (2011).

24. Neglecting α_2 gives the simpler approximation $\Delta T = -2R/3\alpha_1$, but accounting for the temperature dependence of α is necessary, since the resulting correction of $\sim 4\%$ per 100°C is larger than our sensitivity.

25. A. J. C. Wilson, *Proceedings of the Physical Society* **53**, 235 (1941).

26. *See supplementary material* .

27. E.-M. Steyskal, *et al.*, *Physical Review Letters* **108**, 055504 (2012).

28. E. R. White, M. Mecklenburg, B. Shevitski, S. B. Singer, B. C. Regan, *Langmuir* **28**, 3695 (2012).

29. R. F. Egerton, *Reports on Progress in Physics* **72**, 016502 (2009).

30. O. L. Krivanek, *et al.*, *Nature* **514**, 209 (2014).

31. K. A. Gschneidner, *Solid State Physics*, Frederick Seitz and David Turnbull, ed. (Academic Press, 1964), vol. 16, pp. 275–426.